Effect of crack-like defects on the fracture behaviour of Wire + Arc Additively Manufactured nickel-base Alloy 718

Cui E. Seow [a,b,*], Jie Zhang [a], Harry E. Coules [a], Guiyi Wu [c], Christopher Jones [d], Jialuo Ding [e], Stewart Williams [e]

[a] *Department of Mechanical Engineering, University of Bristol, Bristol, BS8 1TR, UK*
[b] *NSIRC, TWI Ltd, Granta Park, Great Abington, Cambridge, CB21 6AL, UK*
[c] *TWI Ltd, Granta Park, Cambridge, CB21 6AL, UK*
[d] *Interface Analysis Centre, University of Bristol, Bristol, BS8 1TR, UK*
[e] *Welding Engineering and Laser Processing Centre, Cranfield University, Cranfield, MK43 0AL, UK*

ABSTRACT

The fabrication of large components using a high deposition rate, near-net shape process like Wire + Arc Additive Manufacturing (WAAM) is a promising option for many industries, due to the potential for reduction in material wastage and shorter lead times in comparison to conventional methods. Specialist materials like nickel-base superalloys, which are typically used in high temperature and corrosive environments, are particularly attractive options due to their high raw material costs. Although nickel-base Alloy 718 seems well suited to the process due to its good weldability, process-induced defects can arise from unfavourable deposition conditions and elimination of these defects may not always be possible. In WAAM Alloy 718 deposited under such conditions, crack-like defects with planar morphology and hot cracking characteristics were observed. These defects were observable using conventional non-destructive testing techniques and displayed directionality relating to the deposition path. The fracture behaviour of WAAM Alloy 718 containing these defects was "semi-stable" – a mixture of fracture instability and stable crack extension. The apparent fracture toughness of WAAM Alloy 718 containing these defects was found to be anisotropic, which can be attributed to the interaction of the notched crack with pre-existing defects. WAAM Alloy 718 displayed an apparent fracture toughness comparable to that of wrought Alloy 718 when notched perpendicular to the defects; but only half that of wrought when notched parallel to the defects. Therefore, careful consideration of defect orientation and their effects on mechanical properties is important in assessing the fitness-for-service of WAAM Alloy 718.

1. Introduction

Wire + Arc Additive Manufacturing (WAAM) is a high-deposition rate, directed energy deposition technique which can be used to build large structures of low to medium complexity [1]. In WAAM, an electric arc is used to simultaneously melt and deposit wire feedstock in a layer-by-layer manner to create a desired geometry. The resulting parts are near-net shape, therefore requiring significantly fewer machining operations in comparison to parts manufactured by conventional methods. This provides material savings and shorter lead times, which are particularly useful for low volume production.

Several alloys can be deposited with WAAM techniques, such as steels [2–4], aluminium [5–7], titanium [8–12] and nickel-base superalloys [13–17]. Nickel-base Alloy 718 is widely used in the aerospace, nuclear, oil and gas industries, due to its high temperature strength and corrosion resistance. The use of WAAM to produce Alloy 718 components is particularly attractive to industry, due to its high raw material cost and difficulty in machining. Alloy 718 is also one of the most weldable (of the commercially available nickel-base superalloys) due to its low Al and Ti contents [18,19], and therefore well-suited for WAAM. The deposition of Alloy 718 has been demonstrated to be viable by several authors. Baufeld [15] and Xu et al. [17] deposited single-pass walls and found that the tensile properties are higher than cast but slightly lower than that of wrought material. Seow et al. [20] reported deposition of thicker sections built using an oscillating deposition strategy, that displayed mechanical properties comparable to cast

---

* Corresponding author.
  E-mail address: cuier.seow@bristol.ac.uk (C.E. Seow).

material. However, all three studies also identified that Alloy 718 is susceptible to micro-segregation during WAAM deposition, which results in microstructural inhomogeneity. Under unfavourable conditions, these can lead to various forms of cracking which may not normally occur in welding.

Severe crack-like defects have been shown to form in WAAM Alloy 718 under unfavourable deposition conditions. Clark et al. [13] reported sinuous crack-like defects in metal-inert-gas (MIG) deposits of Alloy 718. As these defects were found to occur in the overlap region between two deposition passes and did not extend into the final layer, the authors postulated that they had resulted from reheating of previously deposited layers. They also attributed the defect path to the deposited microstructure, specifically the Laves phase "micro-stringers" which formed in the interdendritic regions. Although several suggestions relating to process improvements were made, the authors did not investigate the effects of these defects on mechanical properties of the deposited metal. This is especially important in the development of the WAAM technique for the manufacture of safety critical components.

Interestingly, the occurrence of crack-like defects under unfavourable deposition conditions are not unique to WAAM Alloy 718. Chen et al. [21] reported similar defects in powder-feed laser directed energy deposited (i.e. laser metal deposition) Alloy 718, and attributed their formation to the liquation of low melting point constituents like Laves phase in the microstructure. On the other hand, for Alloy 718 manufactured via powder bed fusion (PBF), crack-like defects are rarely reported as porosity tends to be the dominant defect type [22]. The occurrence of porosity under unfavourable deposition conditions has been demonstrated in laser based [23] and electron beam [24] PBF.

One important mechanical property that drives the design and assessment of safety critical components is fracture toughness. Usually high strength materials have lower toughness, therefore tensile properties alone are insufficient in assessing the suitability of additively manufactured materials. However, there are very few published works on fracture toughness of additively manufactured materials, and most of the published work is on powder-based methods. In a recent review paper, Lewandowski and Seifi [25] reported that although there has been extensive research on uniaxial tensile properties, there are much fewer studies on fracture-critical properties. In addition, most of these studies are on Ti-6Al-4 V, and there are only very few for other alloys such as Alloy 718. Reviewing these, the authors found conflicting results from different studies, attributing them to competing contributions to toughness from microstructure- and defect-dominated effects.

There are a handful of fracture toughness studies of WAAM materials, which report results with varying levels of anisotropy. The toughness of WAAM Ti-6Al-4 V, reported by Zhang et al. [26], was found to be weakly anisotropic; and comparable to that of wrought alloy of the same specimen thickness. The toughness of WAAM high strength low alloy steels, reported by Dirisu et al. [27], was found to be moderately anisotropic, owing to grain size variations in the samples with different notch orientations. Charpy impact toughness of low alloy carbon manganese steels, reported by Sridharan et al. [28], was found to be significantly lower in one build orientation. Although not thoroughly investigated, the authors attributed this to the formation of brittle zones in the microstructure, arising from differences in cooling rates for the different build orientations. The authors of all three studies attributed toughness anisotropy to microstructural effects, but none of them have rigorously investigated the contribution from defect-dominated effects to the fracture toughness results in their studies.

The importance of defect-dominated effects may sometimes be overshadowed by the prospect of eliminating defects in WAAM materials, either through process optimisation or post-deposition treatments. Often, process parameters or deposition strategies can be easily optimised to achieve good deposition. However, under some circumstances these may not be suitable and the complete elimination of defects through process optimisation becomes reliant on trial-and-error, which may vary significantly with deposition equipment and systems. More

robust ways of process optimisation require significant advances in in-process monitoring and an in-depth understanding of microstructural features that control the formation of these defects [25], which are currently only just starting to be investigated. Furthermore, whilst post-deposition treatments like hot isostatic pressing have been demonstrated to reduce defects [29] and result in higher toughness [30], careful consideration of the treatment parameters are necessary to limit undesirable microstructural changes. Such techniques also often have size limitations and will be impractical for the scale of structures that WAAM is intended for. Therefore, pre-existing defects in WAAM may not always be eliminated, and understanding their effects on fracture properties is crucial in assessing their fitness for purpose.

Therefore, the main objectives of this study are to: (i) investigate the microstructural characteristics of crack-like defects formed in WAAM Alloy 718 under unfavourable deposition conditions, (ii) assess the extent to which they form, and (iii) determine their effects on the resulting apparent fracture properties.

2. Methodology

2.1. Material manufacture

WAAM wall samples were manufactured by simultaneously melting and depositing IABCO ERNiFeCr-2 (Alloy 718 filler) wire of 1.14 mm diameter onto a 20 mm thick mild steel substrate plate, using the setup shown in in Fig. 1a. The wire was fed through a wire guide and melted using a plasma torch powered by an EWM Tetrix 352 Synergic plasma controller. A Fanuc Arc mate 120iB robot was programmed to perform the deposition in an oscillating path about the wall axis, as illustrated in Fig. 1b. The robotic arm, plasma torch, deposited sample and sample table were situated within an argon-filled tent. The current and wire feed speed used was 240 A and 2.2 m/s for the first 10 layers. These were gradually changed to 225 A and 3.1 m/s for the remaining layers. The travel speed of the torch was maintained at 6 mm/s throughout the build. The shielding and plasma gas flows were 8 L/min and 0.6 L/min respectively. These parameters were demonstrated to be viable for deposition in previous work [17,31,20] on similar material, although they are not the optimal deposition parameters. Parameter optimisation was not conducted as part of this study. The final build dimensions are shown in Fig. 1b.

The chemical composition of the wire, measured using Inductively Coupled Plasma Optical Emission Spectroscopy (ICP-OES) for major elements and inert gas fusion elemental analysis for C, N and O, is shown in Table 1.

2.2. Defect characterisation

Crack-like defects were identified using dye penetrant inspection, conventional ultrasonic testing, digital X-ray radiography and metallographic techniques. All techniques were performed on wall slices without any post-deposition heat treatment. They were sectioned from the WAAM wall at locations where crack-like defects were the most prominent, shown in Fig. 2. Measurements of crack-like defects were made using image analysis for both techniques.

A water-washable fluorescent dye liquid penetrant (sensitivity level 2) was applied to the surfaces of the WAAM wall sections after they were cleaned in an ultrasonic acetone bath. The walls were soaked for 30 min, then rinsed under clean running water to wash off the excess dye. A developer was applied to the surface and images were taken after 3 min.

Ultrasound measurements were taken using an ultrasonic array (manufactured by Imasonic, Besancon, France) which has 64 elements, a central frequency of 5 MHz, an element width of 0.53 mm and a pitch distance of 0.63 mm. A commercial array controller (Micropulse MP5PA, Peak NDT, Ltd., Derby, UK) was used to capture the time-domain. The captured data was then exported and processed using MATLAB (The MathWorks, Inc., Natick, MA) to generate ultrasonic total
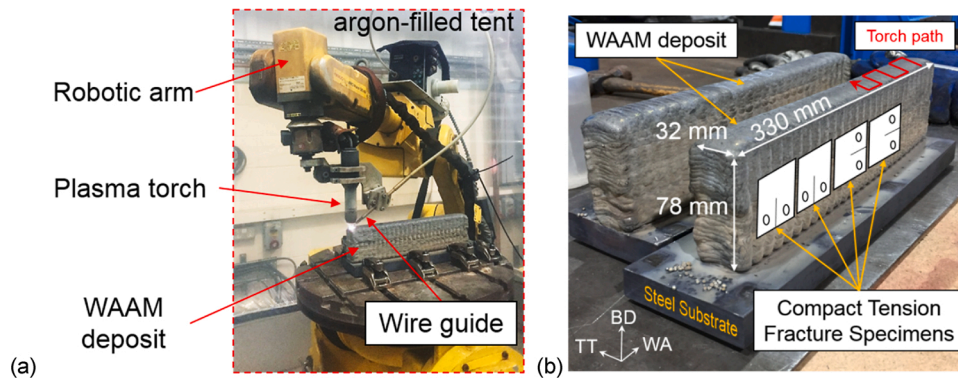
Fig. 1. (a) WAAM equipment and (b) deposited WAAM walls with illustrations of oscillating torch path and fracture specimen extraction locations.

Table 1
Measured chemical composition of IABCO ERNiFeCr-2 filler metal (wt%)

	Ni	Cr	Fe	Nb	Mo	Al	Ti	C	N (ppm)	O (ppm)
IABCO ERNiFeCR-2 (Alloy 718)	55.06	18.02	17.06	4.82	2.82	0.57	0.98	0.04	60	200

This composition is within the SAE International specifications for AMS5383 [32] and AMS5662 [33].
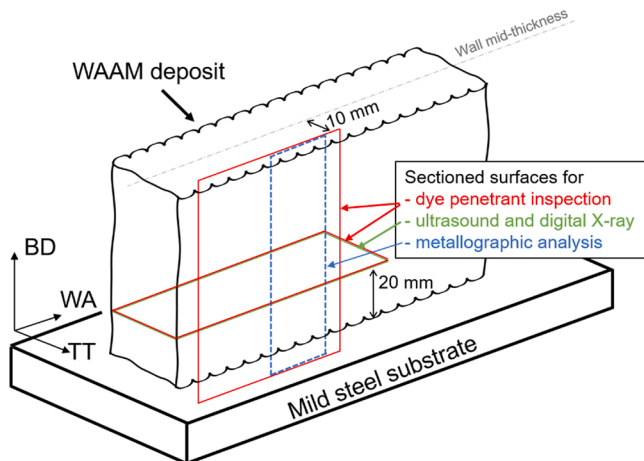

Fig. 2. Schematic showing locations of wall sections extracted for dye penetrant inspection, ultrasonic testing and metallographic analysis.

focusing images [34].

Metallographic specimens were mounted, ground and polished to 0.25 μm. Macro specimens were etched in two parts: (i) electrolytically using 20% H_2SO_4 at 3 V for 10 s for the Alloy 718 deposit, (ii) 3% nital swab for 10 s for the steel substrate. Specimens used in the Scanning Electron Microscope (SEM) were given a final polishing with colloidal silica suspension. Light micrographs were taken using an optical microscope on etched samples. A ZEISS SIGMA field emission gun SEM was used for Energy Dispersive X-ray Spectroscopy (EDX) mapping and Electron Backscatter Diffraction (EBSD). The latter was performed with an Oxford Instruments Nordlys detector, using an accelerating voltage of 30 kV, aperture 60 μm and step size of 3.2 μm.

2.3. Fracture specimens

Fracture samples were heat treated using a specialised homogenisation and aging strategy (1186 °C for 40 min, argon fast cool, 720 °C for 8 h, furnace cool and 620 °C for 8 h, air cool). This heat treatment reduces the microstructural inhomogeneity in WAAM Alloy 718 [20]. As the resulting room temperature tensile properties are weakly anisotropic, the respective direction-specific tensile properties were used in the toughness evaluation described in Section 3.4.

Compact tension (C(T)) specimens, with dimensions shown in Fig. 3, were designed based on guidelines in ASTM E1820-18ae1 [35] and ISO 12135:2016 [36], and sub-sized to optimise the number of specimens extracted per WAAM wall. A pin diameter of 8 mm was used (i.e. Ø 0.2 W instead of 0.188 W or 0.25 W as specified the standards), to achieve a compromise between the (i) amount of material between the integral knife edges and pin holes, and (ii) load bearing capacity of the pins. The specimens were notched in two orientations, parallel and perpendicular to the build direction (i.e. Notch ∥ and Notch ⊥ respectively), as illustrated in Fig. 1b. In addition, C(T) specimens with the same dimensions were extracted from wrought Alloy 718 material
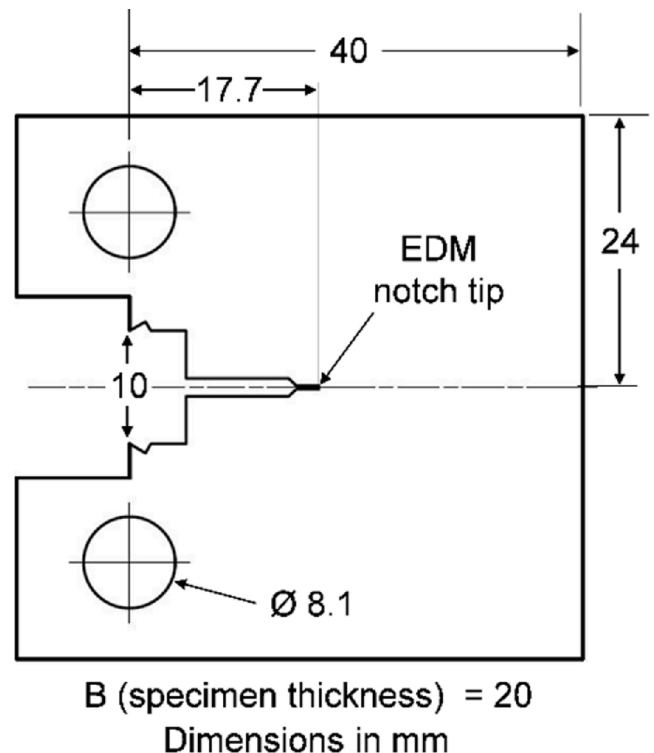

Fig. 3. C(T) specimen machining dimensions before fatigue pre-cracking.

(NACE MR0175 [37], Ø 82.55 mm round bar, solution-treated and age hardened). The C(T) specimens were fatigue pre-cracked to a crack length of 20 mm ($a_0/W = 0.5$). Specimens tested with the basic procedure were plain sided, while specimens tested with the unloading compliance method were side-grooved (10% thickness on each side).

2.4. Fracture testing

Fracture tests were carried out following the procedures outlined in ASTM E1820-18ae1 [35] and ISO 12135:2016 [36], at room temperature. Two test methods were used: the (i) basic procedure and (ii) unloading compliance resistance curve procedure. The former is typically used to obtain single-point fracture toughness values of brittle materials, while the latter is used to determine an engineering estimate of toughness at a small amount of crack extension for ductile materials. For the latter, side-grooved specimens were used. After the test, specimens were heat-tinted, broken open and their fracture surfaces were measured using optical techniques. A summary of test methods and specimens is shown in Table 2.

Toughness measurements were evaluated according to each specimen's response during fracture tests. However, the fracture behaviour of the WAAM C(T) specimens could not be classified as fracture instability or stable crack extension as defined in ASTM E1820-18ae1 [35] and ISO 12135:2016 [36]. Instead, their behaviour can be described as variable decreases in load with increasing displacement, after the attainment of a maximum force, as shown in Fig. 4. This type of behaviour is termed "semi-stable" crack extension throughout this work.

Nonetheless, toughness parameters $J_{m(B)}$, $J_{0.2BL(B)}$ and J_Q were evaluated for the WAAM specimens. The significance of each of these parameters is discussed in Section 3.5. $J_{m(B)}$ was evaluated for specimens tested using the basic procedure and $J_{0.2BL(B)}$ and J_Q were evaluated for specimens tested using the unloading compliance method. $J_{u(B)}$ was evaluated for one specimen which displayed pop-in behaviour. A summary of toughness parameters evaluated is shown in Table 2.

Three of five fracture samples tested using the unloading method displayed an initial decrease in compliance, leading to an apparent "negative crack extension". This has been observed in fracture tests of ductile materials, attributed to crack tip blunting [38] and specimen rotation [39]. Where apparent "negative crack extension" was observed, the vertical axis was shifted to the most negative Δa value, effectively resetting the Δa axis. Although this method is arbitrary, it has been shown to result in the most conservative value of toughness [40]. This adjustment results in toughness values not qualified to the standards. Qualification of toughness values is discussed in Section 3.5.

2.5. Post-test analysis

Prior to being broken open, post-test C(T) specimens were scanned using X-ray computed tomography to visualise the interaction of the main crack with defects through the thickness of the C(T) specimen. Specimens were scanned using a Zeiss XRadia 520 Versa operating at 160 kV, 10 W, with a HE 36 filter, 15 s exposure per projection, and a 100 μm pixel size. Filtered back projection was used to reconstruct a 3D stack showing the internal structure in a non-destructive capability.

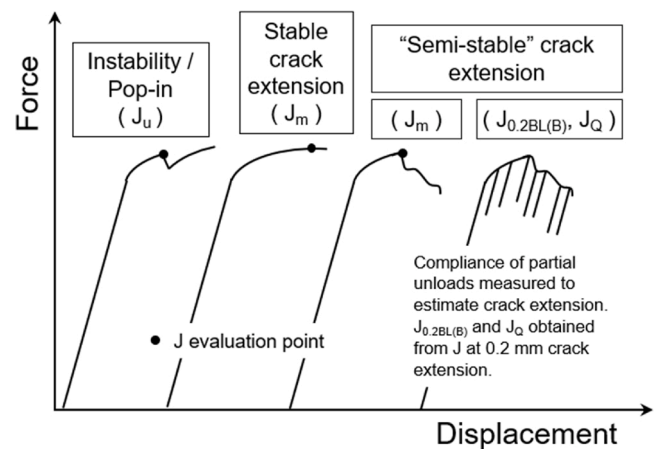**Fig. 4.** Summary of the different types of force-displacement responses from WAAM fracture tests and the corresponding J which were evaluated as per ASTM E1820-18ae1 [35] and ISO 12135:2016 [36].

From this dataset, specific tomogram slices were selected to highlight the crack propagation within the material. After the specimens were scanned, they were heat tinted and broken open. Fractured surfaces of the C(T) specimens were observed using optical techniques, SEM secondary electron imaging and EDX analysis.

3. Results

3.1. Defect morphology and location

Crack-like defects, with a planar morphology normal to the WA direction, were observed to follow a periodic pattern throughout the WAAM walls. They measure up to 16 mm in the TT direction and occur every 12 mm along the wall axis, as shown in the dye penetrant images in Fig. 5a and b. Some defects were also observed to alternate between two TT positions, (i.e. occurring on different sides of the wall), as marked in Fig. 5a. It is important to note that the defects are parallel to the local welding direction in single deposited layer (see illustration in Fig. 5a). Possible reasons for the periodicity and alternating nature of the defects are discussed in Section 4.1. The defects measure up to 53 mm in BD, as shown in the metallographs in Fig. 5c. The stronger fluorescence from the defects Fig. 5a can be attributed to the fact that the defects are longer in the BD direction. The defects were also found located in the centre of the melt bead, as shown in Fig. 6. The characteristics of the defects in relation to the material's microstructure are described in Section 3.2.

3.2. Non-destructive detectability

The non-destructive detectability of sub-surface crack-like defects in WAAM materials is important for quality inspection purposes and crucial to the safe use of components in industry. Two techniques, ultrasound and digital X-ray radiography, were found to be viable in
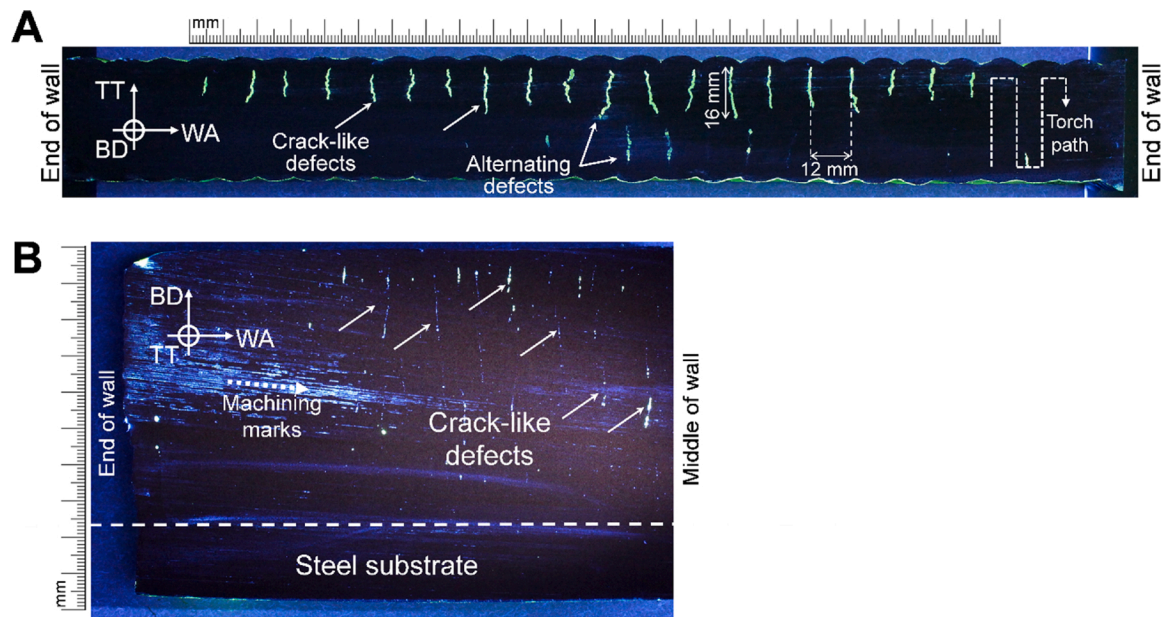
Table 2
Summary of fracture test methods and parameters evaluated

Test method	Side-grooves	Toughness parameter[a]	Material	Notch orientation[b]	No. of Specimens
Basic procedure	No	J_m, J_u	WAAM	∥	6
				⊥	3
			Wrought	-	6
Unloading compliance resistance curve procedure	Yes	J_m, $J_{0.2BL}$, J_Q	WAAM	∥	2
				⊥	2
			Wrought	-	1

[a] for 20 mm specimen thickness
[b] with respect to the WAAM build direction (BD)

Fig. 5. Images from fluorescent dye penetrant testing of WAAM wall sections with planes normal to the (a) build direction (BD) and (b) through thickness (TT) directions.
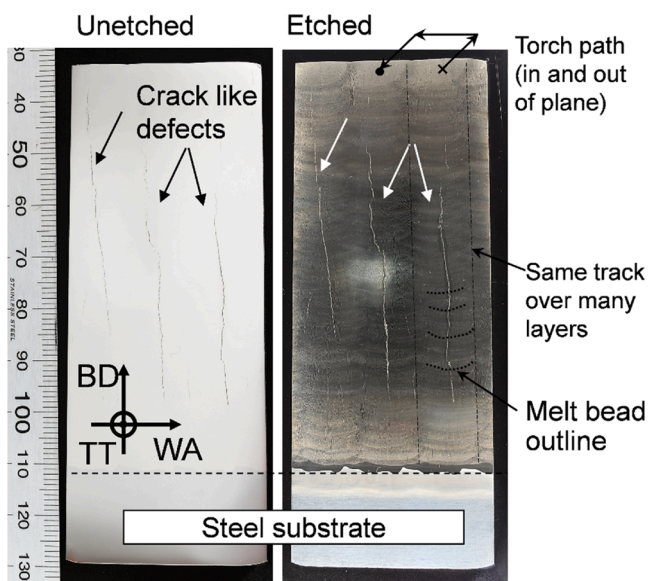

Fig. 6. Metallographs of unetched and etched WAAM wall sections showing the length of the defects in the build direction.

detecting crack-like defects in WAAM Alloy 718. Results from both techniques were found to be in good agreement with measurements from dye penetrant inspection described in Section 3.1.

An illustration of the ultrasound probe and WAAM material setup is shown in Fig. 7a. For ultrasound, the main indicator of the presence of a defect is an amplitude reduction in back wall images. This indication was present in the measurement from a WAAM sample (with defects) but absent in the measurement from a wrought sample (no defects). A plot of the corresponding image amplitudes (at depth of 20 mm) is shown in Fig. 7b. The ultrasound images from the wrought and WAAM materials (i.e. without and with defects) are shown in Fig. 7c and d respectively. Note that the images at a depth around 20 mm is from the back surface of the specimen. As shown, the crack-like defects disturbed the back-surface image and caused a reduction in the image amplitude at a few locations.

The locations with local minimum amplitude in the blue curve indicate the positions of the crack-like defects in the WAAM material. These measurements were repeated on the WAAM slice used for dye penetrant testing. Eight consecutive measurements were made along the WA direction and the combined image amplitude at a depth of 20 mm is shown in Fig. 8b. As shown, the separation distance between the locations with local minimum amplitude is around 12 mm, which is in good agreement with the measurements from dye penetrant testing.

For digital X-ray radiography, indications of the defects were found in the edge-filtered image. The separation distance between the indications is in good agreement with those measured from the dye penetrant image and ultrasound.

3.3. Microstructural characteristics

WAAM Alloy 718 (with or without crack-like defects) has a unique microstructure. The material is made up of long (several mm) columnar grains with strong texture aligned with the build direction. On a sub-grain level, the microstructure can be described as dendritic, with Laves phase decorating the interdendritic regions [17,31,20]. The microstructure of WAAM Alloy 718 deposited under more favourable conditions are described in more detail elsewhere [20]. The following paragraphs will describe the characteristics of crack-like defects in relation to these microstructural features.

The defects were observed to be intergranular, occurring along high-angle grain boundaries, as shown in the EBSD maps in Fig. 9. It is important to note that the strong texture represented in Fig. 9a is with reference to BD. The material has a weaker texture in the other directions (WA and TT), as represented in Fig. 9b. This is known as fibre texture, which has been observed in WAAM Alloy 718 [20]. Fig. 9b shows the defects occurring at high-angle grain boundaries, which are more susceptible to hot cracking [41]. In addition, intragranular misorientation, which is indicative of relative plastic strain [42], was observed in the grains at the tips of the defects (shown in Fig. 9b). This misorientation may have resulted from the rebalancing of strains at the defect tip, shortly after formation of the crack-like defect. The contribution of local strains to the formation of crack-like defects in WAAM is discussed in Section 4.1.

On the sub-grain level, the defects were found in the interdendritic regions of the microstructure, with island-like particles lining their
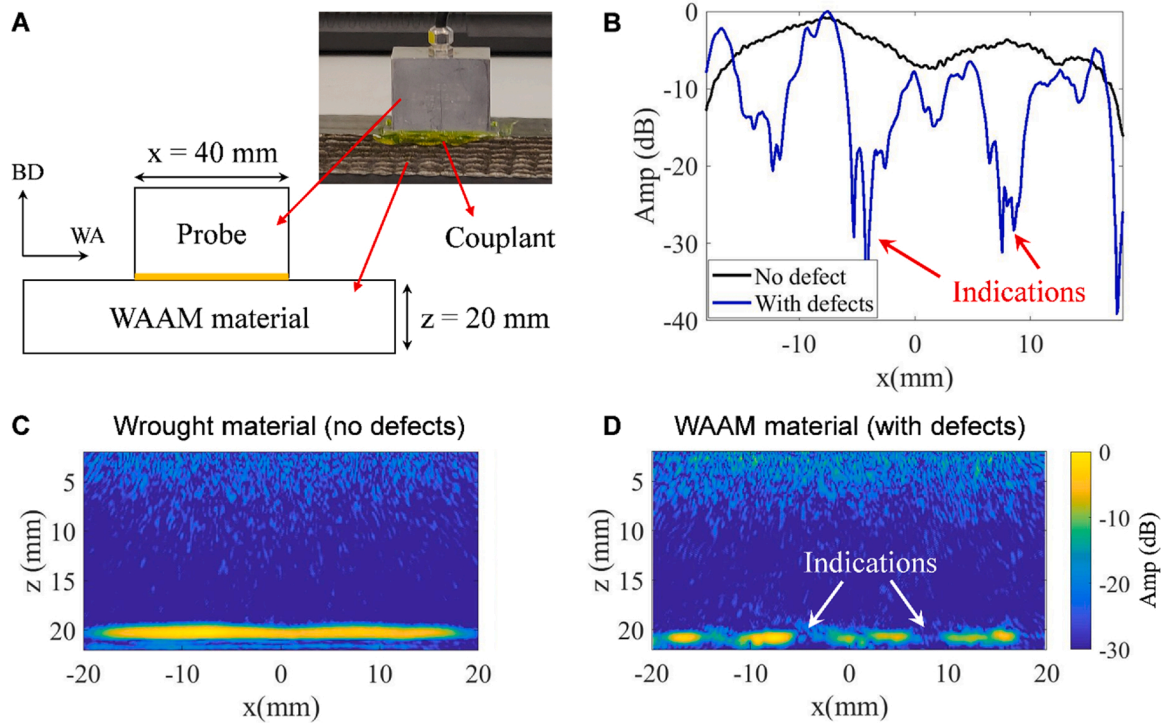
Fig. 7. (a) Illustration of measurement probe and WAAM material setup; (b) ultrasound image amplitude distribution at depth of 20 mm and corresponding ultrasound images of (c) wrought (no defects) and (d) WAAM material (with defects).
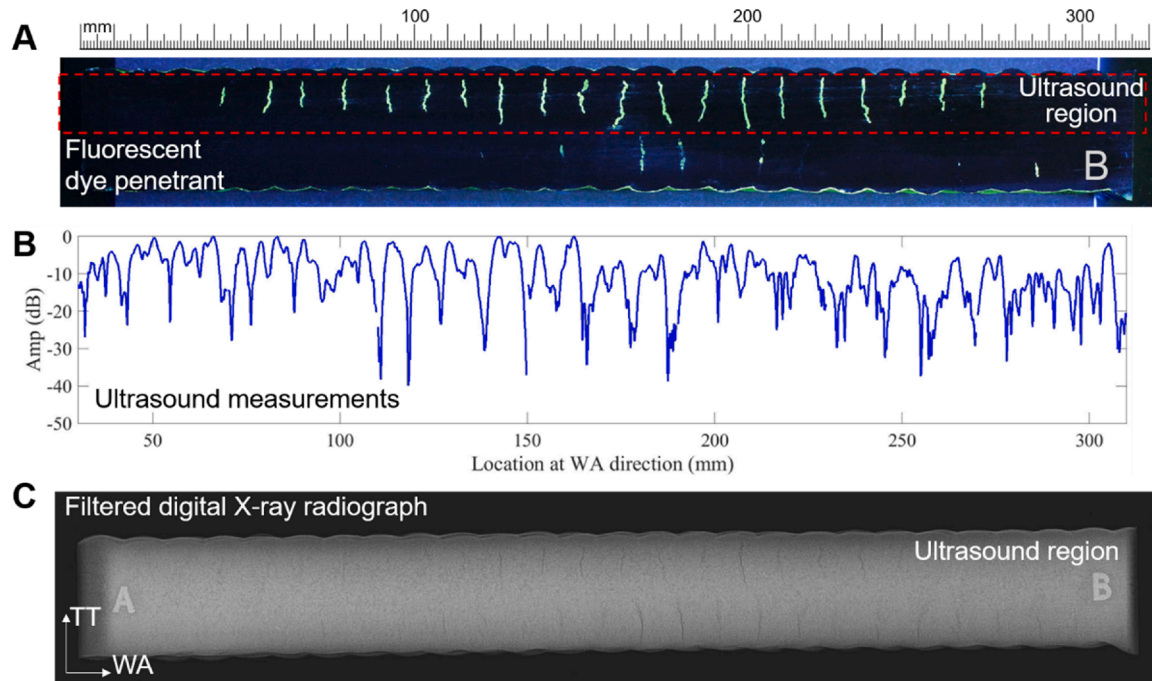

Fig. 8. Non-destructive inspection of crack-like defects; (a) original dye penetrant inspection as shown in Fig. 5a, corresponding (b) combined image amplitude distribution from ultrasound measurements at a depth of 20 mm from 8 consecutive measurements along WA, and (c) edge-filtered digital X-ray radiograph.

edges, as shown in the optical micrographs in Fig. 10. The defects were observed to extend into these particles, and join up with microvoids in the vicinity, as shown in the backscatter electron (BSE) image in Fig. 11a. The EDX maps in Fig. 11b and c confirm that (i) the island-like particles are rich in Nb, characteristic of Laves phase observed in WAAM Alloy 718 [17,20,31]; and (ii) the dark spots in the BSE image ahead of the microfissure are microvoids and not Ti-rich inclusions. These

features indicate the presence of intergranular liquid films which are characteristic of hot cracking [18]. The possible mechanisms of hot cracking in WAAM Alloy 718 are discussed in Section 4.1.

3.4. Fracture toughness measurements

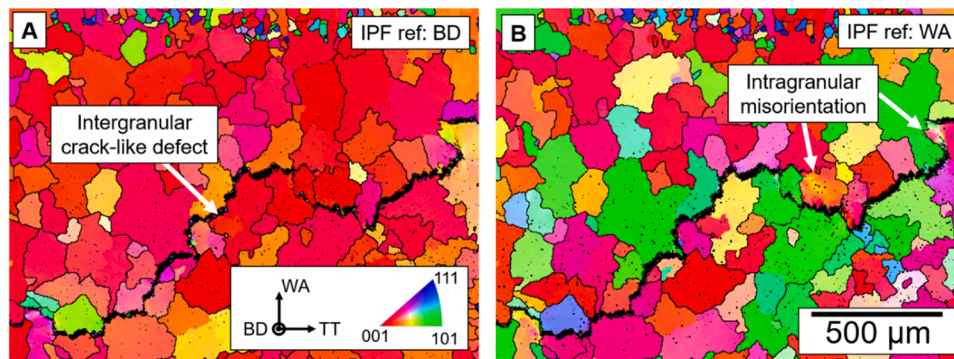The fracture toughness of WAAM Alloy 718 was found to be direction

Fig. 9. EBSD maps of crack-like defects with inverse pole figure (IPF) references in (a) build direction, showing strong texture and intergranular nature of defect; and (b) wall axis direction, showing intragranular misorientations at the tips of the defects.
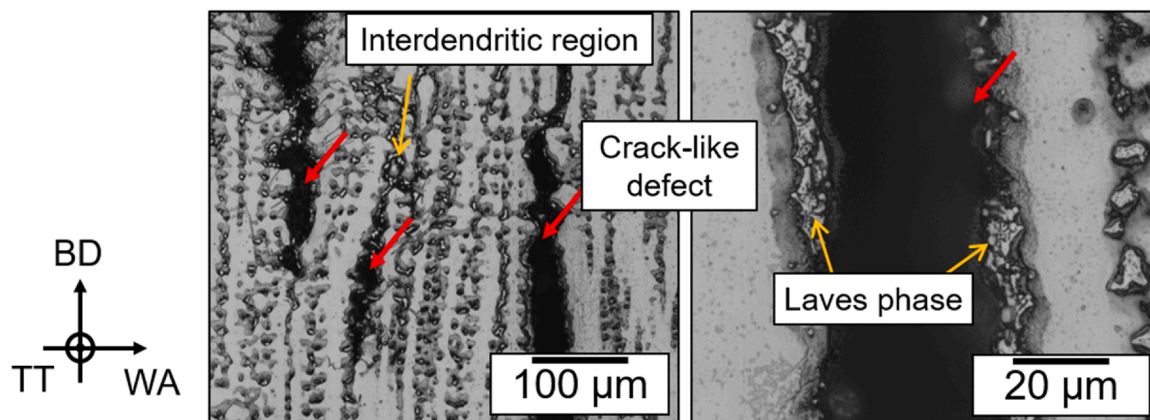

Fig. 10. Optical micrographs of crack-like defects, showing their location in the interdendritic region, and Laves phase particles lining the edges of a defect.

dependent. $J_{m(20)}$, $J_{0.2BL(20)}$ and J_Q, of Notch $\perp$ WAAM Alloy 718 were found to be higher than that of Notch $\parallel$ WAAM Alloy 718. The toughness measurements are plotted in Fig. 12 and summarised in Table 3. The average $J_{m(20)}$, $J_{0.2BL(20)}$ and J_Q of Notch $\perp$ WAAM Alloy 718 were found to be 160, 84 and 101 kJ m^{-2} respectively higher than that of Notch $\parallel$ WAAM Alloy 718. One contributing factor to this direction dependency in toughness is the interaction of crack-like defects with the main crack in the fracture specimens. As the crack-like defects have a plane normal to the WA direction, they are plane parallel and plane perpendicular to the main crack in the Notch $\parallel$ and Notch $\perp$ specimens respectively. The directionality of the crack-like defects with respect to the notch orientation was observed in the fracture surface and X-ray computed tomography slices of the fracture specimens, shown in Section 3.6. Other contributing factors to the direction dependency of toughness are discussed in Section 4.4.

The toughness of Notch $\perp$ WAAM Alloy 718 was found to be comparable to that of wrought Alloy 718. The average $J_{m(20)}$, $J_{0.2BL(20)}$ and J_Q for Notch $\perp$ WAAM Alloy 718, are 110 %, 89 % and 97 % that of wrought Alloy 718. In contrast, the average $J_{m(20)}$, $J_{0.2BL(20)}$ and J_Q of Notch $\parallel$ WAAM Alloy 718 are just 58 %, 51 % and 54 % that of wrought Alloy 718. The higher apparent toughness displayed by Notch $\perp$ WAAM Alloy 718 can be attributed to crack branching effects caused by interactions between the crack-like defects and the main crack. This interaction is discussed in Section 3.6.

Across all specimens, measures of $J_{m(20)}$ are higher than those of $J_{0.2BL(20)}$ and J_Q. This is expected as $J_{m(20)}$ represents toughness at the attainment of maximum load, whereas $J_{0.2BL(20)}$ and J_Q represent toughness at 0.2 mm crack extension, which typically occurs before the specimen attains maximum load. One WAAM Notch $\perp$ specimen displayed pop-in behaviour and the corresponding J_u is 221 kJ m^{-2},

which is comparable to measures of $J_{0.2BL(20)}$ and J_Q of the other Notch $\perp$ specimens.

The WAAM and wrought specimens displayed rising resistance curves, which is characteristic of ductile materials [43]. Example resistance curves for each material type and notch orientation are shown in Fig. 13. Although the corresponding $J_{0.2BL(B)}$ values for the three specimens are similar, they display different resistance curve parameters. The WAAM Notch $\perp$ specimen (Fig. 13b) has a positive vertical intercept and the highest power coefficient. This indicates that the Notch $\perp$ specimen displays the most toughening characteristics with increasing crack extension. In contrast, the WAAM Notch $\parallel$ specimen has a large negative vertical intercept and a power coefficient almost equal to zero. The wrought specimen has resistance curve parameters in-between those of the Notch $\parallel$ and Notch $\perp$ specimens.

3.5. Qualification and significance of toughness measurements

The significance of toughness values reported in Section 3.4 is dependent on the qualification of these values to the criteria outlined in the standards (i.e. ISO 12135:2016 [36] and ASTM E1820-ae1 [35]). None of the toughness values are fully qualified to their respective standards, and the unmet qualification criteria are discussed separately for each toughness parameter. The corresponding specimen description, J values and possible reasons are also detailed in Table 4.

The main issues with qualification of $J_{m(B)}$ (ISO 12135:2016 [36]) were observed in the WAAM specimens and are associated with the fatigue pre-crack and final crack shape. Both can be attributed to the effects of microstructure and crack-like defects. The final crack shape does not directly affect the value of J. In terms of significance, $J_{m(B)}$ represents the "size sensitive fracture resistance J at the first attainment of a
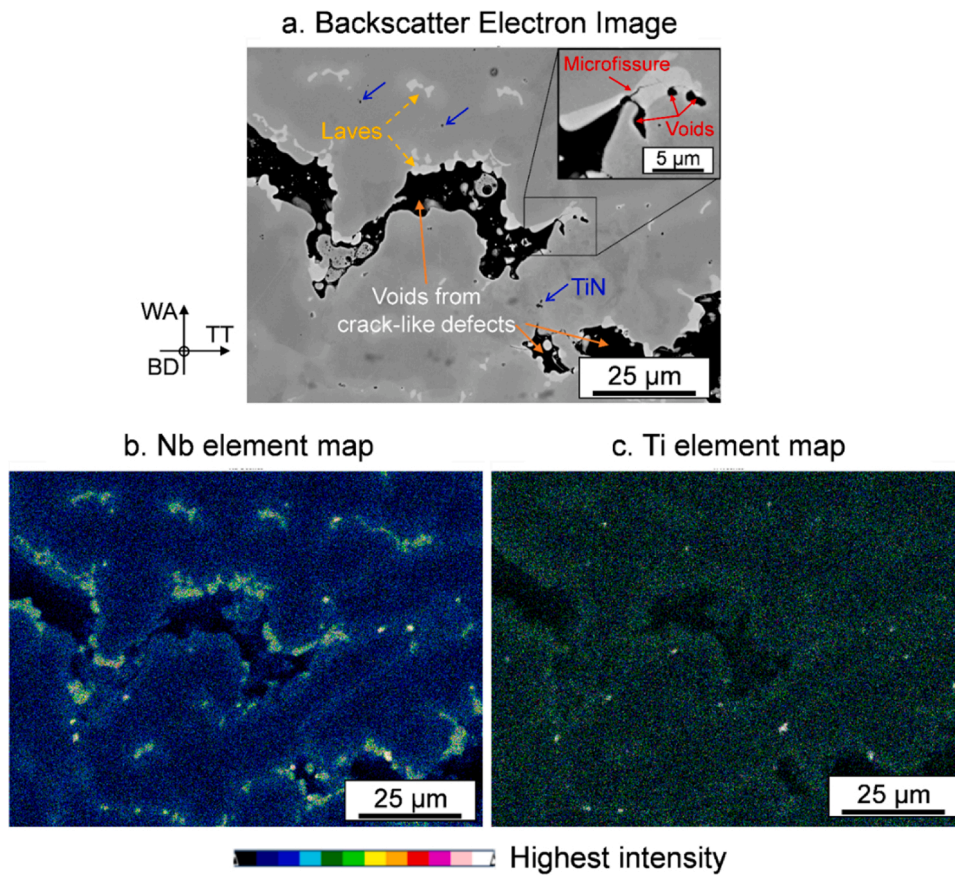
Fig. 11. SEM images of a crack-like defect. (a) BSE image showing a defect extending into Laves phase and joining up with microvoids, (b) and (c) EDX element maps of Nb and Ti respectively.
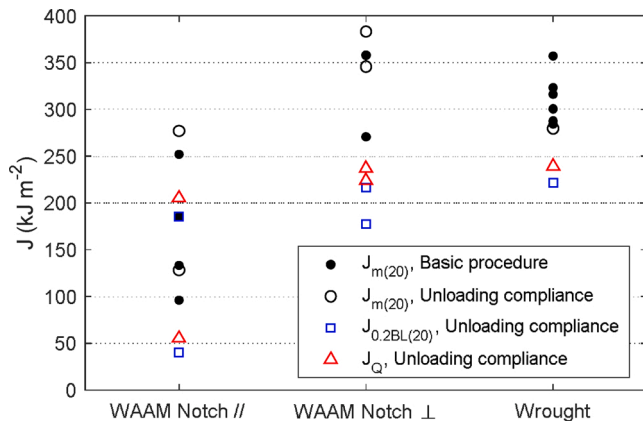

Fig. 12. Toughness measurements of WAAM and wrought specimens. Notch orientations as indicated with respect to the build direction.

Table 3
Summary of toughness measurements for B $=20$ mm (kJ m^{-2})

Material	$J_{m(20)}$	%*	$J_{0.2BL(20)}$	%*	J_Q	%*	$J_{u(20)}$
WAAM Notch ‖	179 ± 73	58	113 ± 103	51	130 ± 106	54	-
WAAM Notch ⊥	339 ± 48	110	197 ± 28	89	231 ± 9	97	221
Wrought	307 ± 28	100	221	100	239	100	-

Note: values listed here refer to the mean and standard deviation of measurements, where applicable.
* percentage of respective wrought properties

maximum force plateau for fully plastic behaviour". It is size sensitive even if all qualification criteria are met.

Issues with qualification of $J_{0.2BL(20)}$ as $J_{0.2BL}$ (ISO 12135:2016 [36]) were observed in both the WAAM and wrought specimens, and are associated with: (i) insufficient data in the third and fourth quadrants, which is a result of ending the fracture tests prematurely due to semi-stable fracture behaviour; (ii) data offset due to apparent "negative crack extension", which is due to crack tip blunting and the offset methodology is described in Section 2.4; and (iii) discrepancies between measured and estimated compliance and crack length, which can be attributed to inaccuracies with the estimated Young's modulus, E, used

in the calculations. Failing these qualification checks, the toughness values cannot be qualified as $J_{0.2BL}$, but they can be represented as $J_{0.2BL(B)}$, which represents the "size sensitive fracture resistance at 0.2 mm stable crack extension offset from the construction line". This can also be interpreted as a thickness-specific engineering estimate of toughness for ductile materials at 0.2 mm of stable crack extension.

As data from the same specimen set was used for the evaluation of J_Q, qualification of J_Q as J_{IC} (ASTM E1820-ae1 [35]) also faced similar issues, associated with insufficient data, data offset along Δa-axis and discrepancies between estimated and measured compliance. Therefore, the toughness values cannot be qualified as J_{IC}, which represents the "toughness of a material near the onset of crack extension from a pre-existing fatigue crack". The significance of J_Q is not outlined in the standard.

Nonetheless, the measures of toughness from the WAAM and wrought specimens described in Section 3.4 can be compared against one another, as they have been obtained from specimens of the same
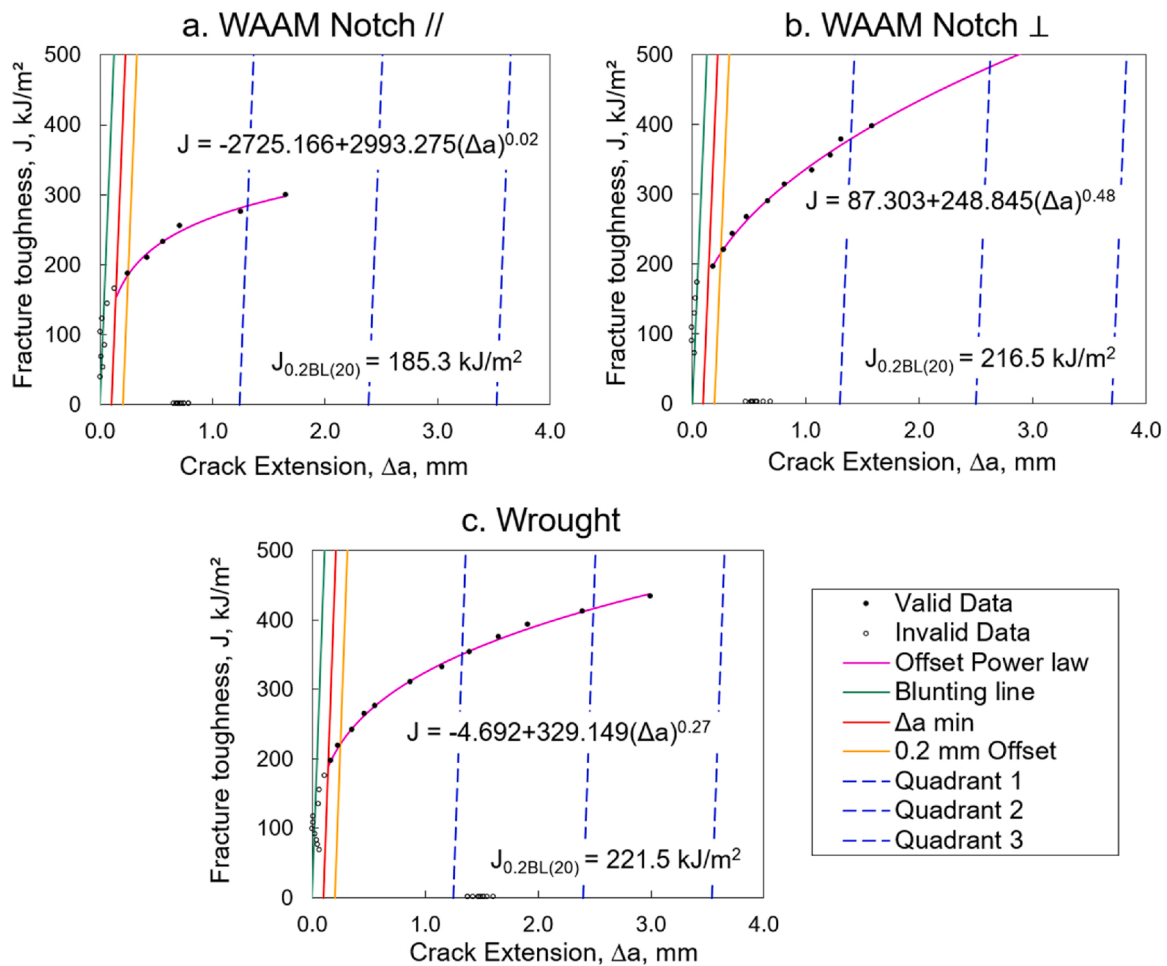
a. WAAM Notch //

$J = -2725.166 + 2993.275(\Delta a)^{0.02}$

$J_{0.2BL(20)} = 185.3 \text{ kJ/m}^2$

b. WAAM Notch ⊥

$J = 87.303 + 248.845(\Delta a)^{0.48}$

$J_{0.2BL(20)} = 216.5 \text{ kJ/m}^2$

c. Wrought

$J = -4.692 + 329.149(\Delta a)^{0.27}$

$J_{0.2BL(20)} = 221.5 \text{ kJ/m}^2$

Legend:
- Valid Data
- Invalid Data
- Offset Power law
- Blunting line
- Δa min
- 0.2 mm Offset
- Quadrant 1
- Quadrant 2
- Quadrant 3

Fig. 13. Resistance curves from WAAM (a) Notch ∥, (b) Notch ⊥ and (c) wrought specimens which displayed similar $J_{0.2BL(20)}$.

thickness (B = 20 mm).

3.6. Post-test crack tip morphology

Evidence of interaction between the crack-like defects and main crack was observed in the fracture surfaces of the WAAM samples, as shown in Fig. 14. The bronze coloured regions are surfaces affected by heat-tinting. This normally consists of the fatigue pre-crack (marked B) and crack extension (marked C), which are typically slightly C-shaped as seen from the wrought specimen. However, in the WAAM specimens, this bronze-coloured region is connected to irregular features (marked E) of the same colour, such as "islands" in the Notch ∥ specimen and out-of-plane cracks in the Notch ⊥ specimen. These features are likely to be crack-like defects which were exposed to the atmosphere during heat-tinting. This interaction between the main crack and defects is confirmed by X-ray computed tomograms of the fracture specimen, described in Section 3.6. Not all crack-like defects were observed to have interacted with the crack extension. The non-interacting defects (marked F) are mostly in the remaining ligament (marked D) of the fracture specimens.

Smooth, liquid-like features were observed on SEM fractographs of a Notch ∥ specimen, as shown in Fig. 15. These features are characteristic of hot cracks, where liquid films form due to liquation of low melting point constituents such as Laves phase or carbides. The possible formation mechanisms of crack-like defects in WAAM Alloy 718 are discussed in Section 4.1.

In the post-test WAAM specimens, crack-like defects were observed to be situated plane parallel and perpendicular with respect to the main crack, for the Notch ∥ and Notch ⊥ specimens respectively as shown in Fig. 16. This indicates that in the Notch ∥ specimen, the crack-like defects close to the propagating crack front results in an extension of the main crack. This secondary crack extension (due to crack-like defects) is essentially a large area of unfused material, which does not contribute to the material's resistance to fracture, thereby leading to a lower apparent fracture toughness. In contrast, these crack-like defects result in deflection of the main crack in the Notch ⊥ specimen. Crack deflection, which is one of several toughening mechanisms in materials [44], effectively reduces the crack driving force [45], leading to a higher apparent fracture toughness.

4. Discussion

4.1. Formation of crack-like defects

The periodic and alternating nature of the defects (see Fig. 17a) can be attributed to the oscillating torch path used in the WAAM deposition. The spacing of alternating defects in WA is 6 mm, which is close to the length of the step advancement, as illustrated in Fig. 17b. The defects alternate above and below the centre-line, and most likely initiated on the returning pass, where the melt pool is enlarged from residual heat of the preceding outward pass [46]. This variation in melt pool geometry may also have an effect on the local strain distribution, which has been observed in numerical models of SLM materials with a similar deposition pattern [47]. This indicates that the implications on defect rate and directionality should be carefully considered when designing a deposition path for WAAM.

Table 4

Summary of qualification criteria which were not met during fracture toughness tests of WAAM and wrought specimens

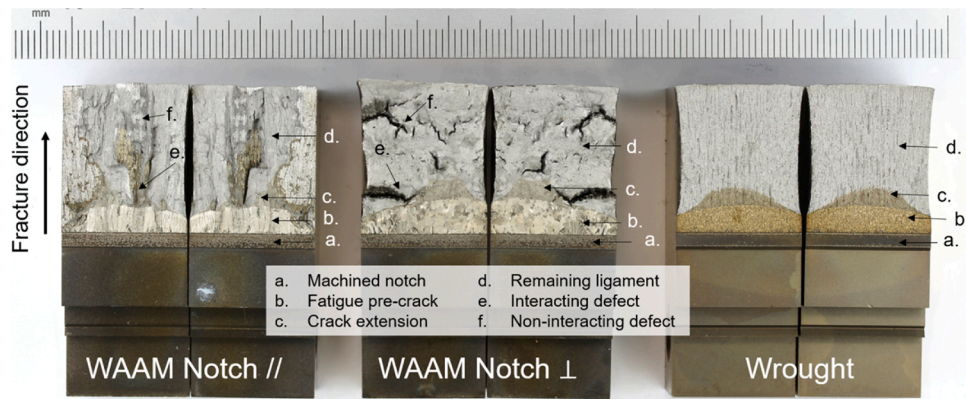| J_m (ISO 12135:2016 [36])	Specimen description	J (kJ m^{-2})	Actual	Allowed	Reason
From basic procedure					
Minimum fatigue pre-crack length (5.8.2 c) (mm)	WAAM Notch ∥	133	0.7	1.3	Interaction of pre-crack with crack-like defect
Fatigue pre-crack within envelope (5.8.2 d)	WAAM Notch ∥	252	-	-	Effect of microstructure
Final crack shape (5.8.3)	All WAAM specimens	-	-	-	Interaction of crack extension with crack like defect and effect of microstructure
From unloading compliance					
Initial K-rate between 0.2 and 3.0 MPa.m$^{0.5}$s^{-1} (5.7.5)	WAAM Notch ∥	128	0.02	0.2 – 3	Specimens tested at slower loading rate than the other specimens
	WAAM Notch ⊥	346	0.02	0.2 – 3	
	Wrought	280	0.14	0.2 – 3	Loading rate decreased due to pin shear challenges
Fatigue pre-crack within envelope (5.8.2 d)	WAAM Notch ⊥	346	-	-	Effect of microstructure on the path of the fatigue pre-crack
	Wrought	280	-	-	
$J_{0.2BL}$ (ISO 12135:2016 [36])	**Specimen description**	**J (kJ m^{-2})**	**Actual**	**Allowed**	**Reason**
Fit coefficient α greater or equal to 0.0 (7.4.2.2)	WAAM Notch ∥	185	−2725	≥0.0	
	WAAM Notch ⊥	177	−172	≥0.0	A result of "negative" crack extension, which affects the shape of the R-curve and hence fitting parameters
	Wrought	211	−4.7	≥0.0	
At least 1 valid data point in each quadrant (7.4.2.2)	WAAM Notch ∥	185	-	-	
	WAAM Notch ⊥	177	-	-	Insufficient data. Test stopped before crack extension reached third quadrant due to (i) fracture instabilities, (ii) specimen peak load achieved before sufficient crack extension
	WAAM Notch ⊥	217	-	-	
	Wrought	211	-	-	
Esimated final crack length (7.2.3) (mm)	WAAM Notch ∥	185	0.93	1.58 – 2.14	
	WAAM Notch ⊥	177	1.95	2.05 – 2.78	Inaccuracies in estimated E and/or measured compliance reduced by crack-like defect
	Wrought	221	1.52	2.36 – 3.19	
Data offset along Δa axis (mm)	WAAM Notch ∥	185	−0.73	0	
	WAAM Notch ⊥	217	−0.57	0	To address "negative" crack extension caused by crack tip blunting
	Wrought	211	−1.48	0	
λ within 10% of specimen unloading compliance (H.5.1)	All specimens	-	-	-	Inaccuracies in estimated E and/or measured compliance reduced by crack-like defect
J_{IC} (ASTM E 1820-ae1 [35])	**Specimen description**	**J (kJ m^{-2})**	**Actual**	**Allowed**	**Reason**
Correlation coefficient of fit ≥ 0.96 (A9.3.3.2)	WAAM Notch ∥	55	0.12	≥ 0.96	Differences between measured and estimated initial specimen compliance
	WAAM Notch ⊥	224	0.70	≥ 0.96	
No of points used to calculate a0q ≥ 3 between 0.4J_Q and J_Q (A9.3.3.2)	WAAM Notch ∥	205	0	≥ 3	Insufficient data. Test stopped as peak load achieved before reaching maximum crack extension capacity of specimen.
	WAAM Notch ⊥	237	2	≥ 3	
	Wrought	239	0	≥ 3	
Data offset along Δa axis (mm)	WAAM Notch ∥	205	−0.73	0	
	WAAM Notch ⊥	237	−0.56	0	To address "negative" crack extension caused by crack tip blunting
	Wrought	239	−1.48	0	

Fig. 14. Fracture surfaces of WAAM and wrought C(T) specimens. Bronze colour indicates exposed surfaces during heat-tinting (i.e. fatigue pre-crack, crack extension and defects).
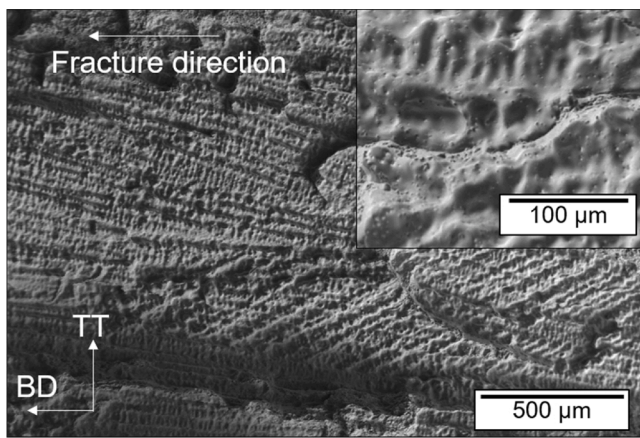

Fig. 15. SEM secondary electron image of a crack-like defect from the fracture surface of Notch ‖ specimen, showing solidified liquid film characteristic of hot cracking.

The characteristics of the crack-like defects described in Section 3.3 resemble aspects of hot cracking in welds, which can be attributed to two mechanisms – solidification and liquation cracking. Both mechanisms are associated with the presence of intergranular liquid films, but the former usually results from restraint, which may be present in thick WAAM deposits. The latter, which results from liquation of low melting point constituents in the microstructure [48], can occur in WAAM due to

the reheating of deposited material. WAAM Alloy 718 is especially susceptible to liquation cracking due to the presence of Laves phase and NbC in the microstructure. The Nb-rich Laves phase along the edges of the defects described in Section 3.2 could be a product of the re-solidification of liquated low-melting-point constituents [49]. The hot cracking mechanism in WAAM Alloy 718 is likely to be a combination of both solidification and liquation cracking. Therefore, strategies to mitigate the formation intergranular liquid films and restraint must be adopted to minimise the formation of crack-like defects. Some of these strategies are discussed in Section 4.3.

4.2. Detecting crack-like defects

The non-destructive detectability of crack-like defects in WAAM Alloy 718 is important for quality inspection purposes. Although dye penetrant inspection, conventional ultrasound testing and X-ray radiography were shown in Section 3.2 to be suitable for detection of crack-like defects, each technique has their limitations. Dye penetrant testing is limited to surface breaking defects and can be sensitive to surface artefacts. Conventional ultrasonic testing requires a smooth surface for good coupling and is limited in characterising defect size. X-ray radiography may not be feasible for large parts or thick sections. In addition, for all three techniques defect size and orientation can also affect the inspection results, therefore quality inspections must be conducted in consideration of these factors.

Non-destructive defect detection techniques can also be beneficial for process optimisation when conducted in-situ with deposition. There are a few monitoring and inspection techniques suitable for
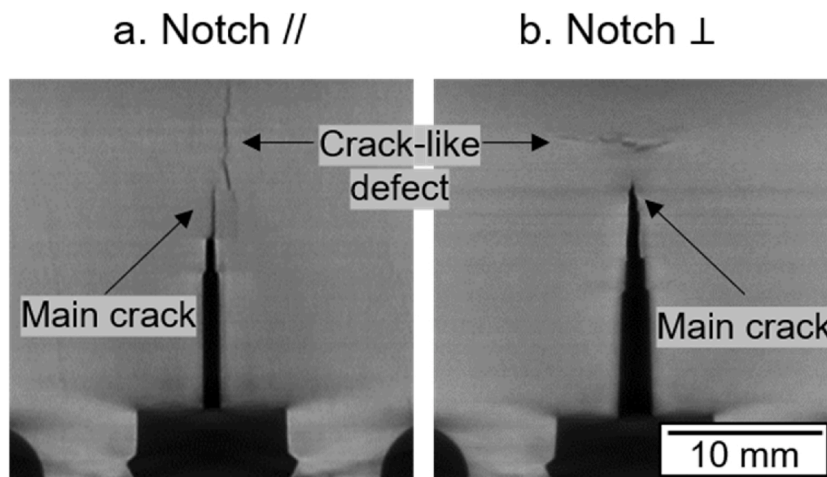

Fig. 16. X-ray tomograms, acquired at 160 kV with filtering, of post test WAAM (a) Notch ‖ and (b) Notch ⊥ specimens.
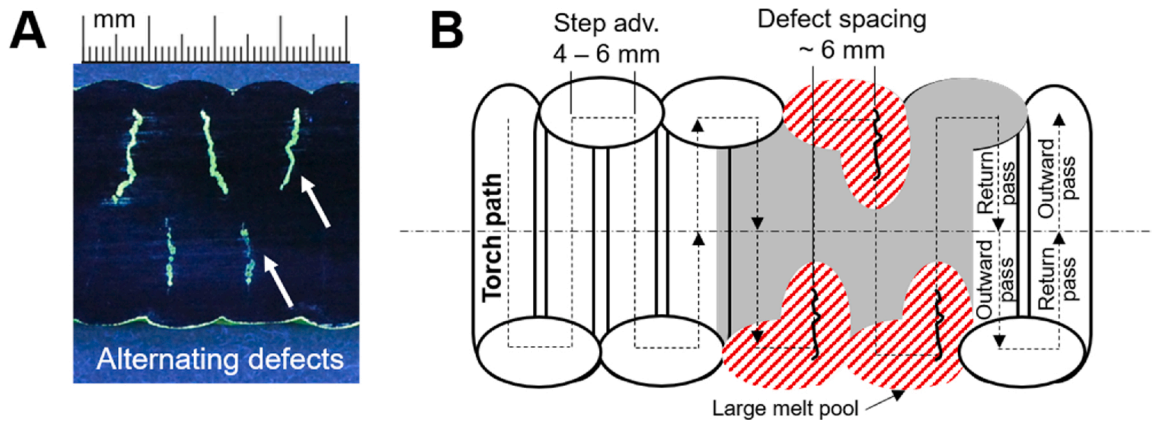
Fig. 17. (a) Insert from Fig. 5 showing alternating defects. (b) Schematic of possible hot and cool zones resulting from the oscillating tool path, leading to alternating defect pattern.

implementation during the WAAM process, which have been broadly reviewed by Lopez et al. [50]. They include eddy current, electromagnetic and laser ultrasonic testing, which may provide a way forward for production quality feedback control.

4.3. Mitigating crack-like defects

Mitigation of crack-like defects is mainly dependent on the ability to limit two effects: (i) the formation of low melting point constituents such as Laves phase and carbides in the microstructure; and (ii) the build-up of localised strain in the deposited material. Both are strongly affected by thermal conditions during deposition. One way to manage this is to lower the heat input, which has been observed to reduce hot cracking susceptibility in multi-pass weldments of cast Alloy 718 [51]. Control of heat input can be achieved by adapting the deposition strategy, such as using parallel rather than oscillating torch paths. Lower heat input can also be achieved by adjusting the WAAM primary input process parameters (i.e. current, contact-tip-to-work distance, travel speed, wire feed speed and gas flow rates.), although changing these parameters can also alter weld bead geometry, requiring re-optimisation to maintain process stability and geometric control. An alternative which circumvents this is to limit the inter-pass temperature, which has been observed to reduce porosity in WAAM Al alloy [52]. However, this may introduce a wait time between each pass, which adds to the overall build time. There are also various ancillary processes that can be implemented in-situ to control thermal conditions. These have been comprehensively reviewed by Cunningham et al. [53] and Oliveira et al. [54], and are based on the following general principles: (i) reducing heat input into the workpiece – through pulsed current [55] and hot-wire deposition [56] techniques; (ii) dissipating heat away from the workpiece – through local cooling to the weld pool [57,58], substrate cooling [59,60], or inter-layer forced cooling [61,62]; (iii) weld pool agitation – through ultrasonic vibration [63,64] and arc oscillation [65,66] techniques.

The build-up of localised strain can also be mitigated by reducing restraint and residual stress build up. Some techniques that address these are based on the following principles: (i) plastic deformation and grain refinement – through inter-layer high pressure cold rolling [67] and laser shock peening [68] and (ii) geometrical considerations – through deposition path optimisation [69–71], or component and build design optimisation [72].

At present, optimisation of parameters of primary and ancillary processes relies heavily on trial-and-error, which is not feasible at production scales. Feedback control of such parameters is crucial in process optimisation. One way of achieving feedback control is through in-situ temperature monitoring. Transient thermal profiles of WAAM deposits have been achieved with infrared thermography [73], although the technique was unable to accurately capture the thermal profile of the
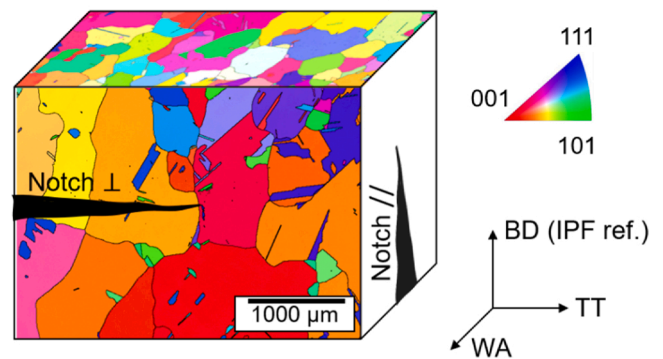

Fig. 18. Notch orientations of WAAM C(T) fracture specimens in relation to WAAM Alloy 718 material grain structure. EBSD maps show high-angle grain boundaries and grain orientation in IPF colouring.

weld pool. Lastly, although costly and time consuming, modifications to the alloy composition can be made to further manipulate solidification kinetics.

4.4. Other factors influencing the direction dependence of fracture toughness

The direction dependence of fracture toughness reported in Section 3.4 has been largely attributed to the interaction between crack-like defects and the main propagating crack of the fracture specimen. Whilst this has been shown to occur in the post-test analysis described in Section 3.6, there may be other sources contributing to the direction dependency of toughness measurements. From a microstructural viewpoint, the grain structure of the WAAM Alloy 718 material (after heat treatment) is anisotropic, as shown in Fig. 18. The main crack in a WAAM Notch ∥ specimen propagates along the long axis of the grains. Therefore, in the absence of crack-like defects in the WAAM Alloy 718 material, toughness measurements are still likely to be direction dependent.

5. Conclusions

The following conclusions can be drawn from this work:

1 Crack-like defects with planar morphology can form in WAAM Alloy 718 under unfavourable deposition conditions. The defect pattern can be attributed to the WAAM deposition path.

2 These defects have hot cracking characteristics. They occur in the centre of the melt bead, along high-angle grain boundaries and have edges lined with Laves phase.

3 Non-destructive detection of these defects is feasible using dye penetrant, conventional ultrasonic and X-ray radiography techniques.

4 The material's fracture toughness was observed to be anisotropic, depending on notch orientation with respect to the defects. When notched plane perpendicular to defects, WAAM Alloy 718 has apparent toughness comparable to wrought Alloy 718. However, when notched plane parallel to defects, toughness of WAAM Alloy 718 is half that of wrought Alloy 718.

This work demonstrates that the orientation of crack-like defects can have a large effect on the resulting apparent fracture toughness of WAAM Alloy 718. The effect of direction dependence should be an important consideration at various stages of materials characterisation for WAAM materials. In addition, direction dependent fracture properties may have implications on structural integrity assessments.

CRediT authorship contribution statement

Cui E. Seow: Conceptualisation, Investigation, Writing - original draft, Visualisation. **Jie Zhang:** Investigation, Writing - review & editing, Resources. **Harry E. Coules:** Supervision, Conceptualisation, Resources, Funding acquisition, Writing - review & editing. **Guiyi Wu:** Supervision, Conceptualisation, Resources, Funding acquisition, Writing - review & editing. **Christopher Jones:** Investigation, Resources. **Jialuo Ding:** Resources. **Stewart Williams:** Resources, Writing - review & editing.

Declaration of Competing Interest

The authors declare that they have no known competing financial interests or personal relationships that could have appeared to influence the work reported in this paper.

References

[1] S.W. Williams, F. Martina, A.C. Addison, J. Ding, G. Pardal, P. Colegrove, Wire + arc additive manufacturing, Mater. Sci. Technol. 32 (7) (2016) 641–647.

[2] C.V. Haden, G. Zeng, F.M. Carter, C. Ruhl, B.A. Krick, D.G. Harlow, Wire and arc additive manufactured steel: Tensile and wear properties, Addit. Manuf. 16 (August) (2017) 115–123.

[3] F. Martina, J. Ding, S. Williams, A. Caballero, G. Pardal, L. Quintino, Tandem metal inert gas process for high productivity wire arc additive manufacturing in stainless steel, Addit. Manuf. 25 (January) (2019) 545–550.

[4] X. Xu, S. Ganguly, J. Ding, S. Guo, S. Williams, F. Martina, Microstructural evolution and mechanical properties of maraging steel produced by wire + arc additive manufacture process, Mater. Charact. 143 (September) (2018) 152–162.

[5] B. Cong, J. Ding, S. Williams, Effect of arc mode in cold metal transfer process on porosity of additively manufactured Al-6.3%Cu alloy, Int. J. Adv. Manuf. Technol. 76 (9–12) (2015) 1593–1606.

[6] A. Horgar, H. Fostervoll, B. Nyhus, X. Ren, M. Eriksson, O.M. Akselsen, Additive manufacturing using WAAM with AA5183 wire, J. Mater. Process. Technol. 259 (September) (2018) 68–74.

[7] P.A. Colegrove, J. Donoghue, F. Martina, J. Gu, P. Prangnell, J. Hönnige, Application of bulk deformation methods for microstructural and material property improvement and residual stress and distortion control in additively manufactured components, Scr. Mater. 135 (2017) 111–118.

[8] B. Baufeld, E. Brandl, O. Van Der Biest, Wire based additive layer manufacturing: Comparison of microstructure and mechanical properties of Ti-6Al-4V components fabricated by laser-beam deposition and shaped metal deposition, J. Mater. Process. Technol. 211 (6) (2011) 1146–1158.

[9] F. Wang, S. Williams, M. Rush, Morphology investigation on direct current pulsed gas tungsten arc welded additive layer manufactured Ti6Al4V alloy, Int. J. Adv. Manuf. Technol. 57 (5–8) (2011) 597–603.

[10] F. Wang, S. Williams, P. Colegrove, A.A. Antonysamy, Microstructure and mechanical properties of wire and arc additive manufactured Ti-6Al-4V, Metall. Mater. Trans. A 44 (2) (2013) 968–977.

[11] F. Martina, J. Mehnen, S.W. Williams, P. Colegrove, F. Wang, Investigation of the benefits of plasma deposition for the additive layer manufacture of Ti-6Al-4V, J. Mater. Process. Technol. 212 (June 6) (2012) 1377–1386.

[12] B. Baufeld, O. Van der Biest, R. Gault, Manufacturing of Ti-6Al-4V components by shaped metal deposition: Microstructure and mechanical properties, Mater. Des. 31 (SUPPL. 1) (2010).

[13] D. Clark, M.R. Bache, M.T. Whittaker, Shaped metal deposition of a nickel alloy for aero engine applications, J. Mater. Process. Technol. 203 (1–3) (2008) 439–448.

[14] D. Clark, M.R. Bache, M.T. Whittaker, Microstructural characterization of a polycrystalline nickel-based superalloy processed via tungsten-inert-gas-shaped metal deposition, Metall. Mater. Trans. B 41 (6) (2010) 1346–1353.

[15] B. Baufeld, Mechanical properties of INCONEL 718 parts manufactured by shaped metal deposition (SMD), J. Mater. Eng. Perform. 21 (7) (2012) 1416–1421.

[16] G. Asala, A.K. Khan, J. Andersson, O.A. Ojo, Microstructural Analyses of ATI 718Plus® Produced by Wire-ARC Additive Manufacturing Process, Metall. Mater. Trans. A 48 (9) (2017) 4211–4228.

[17] X. Xu, J. Ding, S. Ganguly, S. Williams, Investigation of process factors affecting mechanical properties of INCONEL 718 superalloy in wire + arc additive manufacture process, J. Mater. Process. Technol. 265 (March) (2019) 201–209.

[18] J.N. DuPont, J.C. Lippold, S.D. Kiser, Precipitation-Strengthened Ni-base Alloys. Welding Metallurgy and Weldability of Nickel-Base Alloys, John Wiley & Sons, Inc., 2009, pp. 157–254.

[19] M.J. Donachie, S.J. Donachie, Superalloys: A Technical Guide, 2nd Edition, ASM International, 2002.

[20] C.E. Seow, H.E. Coules, G. Wu, R.H.U. Khan, X. Xu, S. Williams, Wire + Arc Additively Manufactured Inconel 718: Effect of post-deposition heat treatments on microstructure and tensile properties, Mater. Des. 183 (September) (2019) 108157. December.

[21] Y. Chen, K. Zhang, J. Huang, S.R.E. Hosseini, Z. Li, Characterization of heat affected zone liquation cracking in laser additive manufacturing of Inconel 718, Mater. Des. 90 (2016) 586–594.

[22] E. Hosseini, V.A. Popovich, A review of mechanical properties of additively manufactured Inconel 718, Additive Manufacturing 30 (Elsevier B.V) (2019) 100877, 01-Dec-10.

[23] K. Georgilas, R.H.U. Khan, M.E. Kartal, The influence of pulsed laser powder bed fusion process parameters on Inconel 718 material properties, Mater. Sci. Eng. A 769 (January) (2020) 138527.

[24] A. Strondl, M. Palm, J. Gnauk, G. Frommeyer, Microstructure and mechanical properties of nickel based superalloy IN718 produced by rapid prototyping with electron beam melting (EBM), Mater. Sci. Technol. 27 (May 5) (2011) 876–883.

[25] J.J. Lewandowski, M. Seifi, Metal Additive Manufacturing: A Review of Mechanical Properties, Annu. Rev. Mater. Res. 46 (1) (2016) 151–186.

[26] X. Zhang, F. Martina, J. Ding, X. Wang, S.W. Williams, Fracture toughness and fatigue crack growth rate properties in wire + arc additive manufactured Ti-6Al-4V, Fatigue Fract. Eng. Mater. Struct. 40 (May 5) (2017) 790–803.

[27] P. Dirisu, S. Ganguly, A. Mehmanparast, F. Martina, S. Williams, Analysis of fracture toughness properties of wire + arc additive manufactured high strength low alloy structural steel components, Mater. Sci. Eng. A 765 (2019).

[28] N. Sridharan, M.W. Noakes, A. Nycz, L.J. Love, R.R. Dehoff, S.S. Babu, On the toughness scatter in low alloy C-Mn steel samples fabricated using wire arc additive manufacturing, Mater. Sci. Eng. A 713 (January) (2018) 18–27.

[29] L.N. Carter, C. Martin, P.J. Withers, M.M. Attallah, The influence of the laser scan strategy on grain structure and cracking behaviour in SLM powder-bed fabricated nickel superalloy, J. Alloys Compd. 615 (December) (2014) 338–347.

[30] M. Seifi, A.A. Salem, D.P. Satko, U. Ackelid, S.L. Semiatin, J.J. Lewandowski, Effects of HIP on microstructural heterogeneity, defect distribution and mechanical properties of additively manufactured EBM Ti-48Al-2Cr-2Nb, J. Alloys Compd. 729 (2017) 1118–1135.

[31] X. Xu, S. Ganguly, J. Ding, C.E. Seow, S. Williams, Enhancing mechanical properties of wire + arc additively manufactured INCONEL 718 superalloy through in-process thermomechanical processing, Mater. Des. 160 (December) (2018) 1042–1051.

[32] SAE International, AMS5383F Nickel Alloy, Corrosion and Heat-Resistant, Investment Castings 52.5Ni - 19Cr - 3.0Mo - 5.1Cb(Nb) - 0.90Ti - 0.60Al - 18Fe Vacuum Melted Homogenization and Solution Heat Treated, SAE International, 2018.

[33] SAE International, AMS5662N Nickel Alloy, Corrosion and Heat-Resistant, Bars, Forgings, and Rings 52.5Ni - 19Cr - 3.0Mo - 5.1Cb (Nb) - 0.90Ti - 0.50Al - 18Fe Consumable Electrode or Vacuum Induction Melted 1775 °F (968 °C) Solution Heat Treated, Precipitation-Hardenable, SAE International, 2016.

[34] C. Holmes, B.W. Drinkwater, P.D. Wilcox, Post-processing of the full matrix of ultrasonic transmit-receive array data for non-destructive evaluation, NDT E Int. 38 (December 8) (2005) 701–711.

[35] ASTM International, ASTM E1820-18ae1 Standard Test Method for Measurement of Fracture Toughness, ASTM International, West Conshohocken, PA, 2018.

[36] ISO, ISO 12135:2016 Metallic materials — Unified method of test for the determination of quasistatic fracture toughness, ISO, Geneva, Switzerland, 2016.

[37] NACE International, ANSI/NACE MR0175/ISO 15156-2015-SG Petroleum and natural gas industries — Materials for use in H2S-containing environments in oil and gas production, NACE International, Houston, TX, 2015.

[38] K. Weiss, A. Nyilas, Specific aspects on crack advance during J-test method for structural materials at cryogenic temperatures, Fatigue Fract. Eng. Mater. Struct. 29 (2) (2006) 83–92.

[39] M.A. Verstraete, S. Hertelé, R.M. Denys, K. Van Minnebruggen, W. De Waele, Evaluation and interpretation of ductile crack extension in SENT specimens using unloading compliance technique, Eng. Fract. Mech. 115 (January) (2014) 190–203.

[40] Y. Rosenthal, R. Tobler, P. Purtscher, JIc Data Analysis Methods with a 'Negative Crack Growth' Correction Procedure, J. Test. Eval. 18 (4) (1990) 301.

[41] N. Wang, S. Mokadem, M. Rappaz, W. Kurz, Solidification cracking of superalloy single- and bi-crystals, Acta Mater. 52 (June 11) (2004) 3173–3182.

[42] S.I. Wright, M.M. Nowell, D.P. Field, A review of strain analysis using electron backscatter diffraction, Microsc. Microanal. 17 (June 3) (2011) 316–329.

[43] M.E. Launey, R.O. Ritchie, On the Fracture Toughness of Advanced Materials, 1999.

[44] R.O. Ritchie, The conflicts between strength and toughness, Nat. Mater. 10 (November 11) (2011) 817–822.

[45] R.O. Ritchie, Mechanisms of fatigue crack propagation in metals, ceramics and composites: Role of crack tip shielding, Mater. Sci. Eng. 103 (1) (1988) 15–28.

[46] A. Plotkowski, M.M. Kirka, S.S. Babu, Verification and validation of a rapid heat transfer calculation methodology for transient melt pool solidification conditions in powder bed metal additive manufacturing, Addit. Manuf. 18 (December) (2017) 256–268.

[47] A. Ukwattage, A. Achuthan, Development of residual stress in parts fabricated via selective laser melting (SLM) technique under different scanning strategies, AIAA/ASCE/AHS/ASC Structures, Structural Dynamics, and Materials Conference, 2018 (2018) no. 210049.

[48] R.G. Thompson, D.E. Mayo, B. Radhakrishnan, The relationship between carbon content, microstructure, and intergranular liquation cracking in cast nickel alloy 718," *Metall*, Trans. A 22 (February 2) (1991) 557–567.

[49] R.G. Thompson, S. Genculu, Microstructural Evolution in the HAZ of Inconel 718 and Correlation with the Hot Ductility Test, Weld. J. 62 (12) (1983) 337–345.

[50] A. Lopez, R. Bacelar, I. Pires, T.G. Santos, J.P. Sousa, L. Quintino, Non-destructive testing application of radiography and ultrasound for wire and arc additive manufacturing, Addit. Manuf. 21 (May) (2018) 298–306.

[51] X. Ye, X. Hua, M. Wang, S. Lou, Controlling hot cracking in Ni-based Inconel-718 superalloy cast sheets during tungsten inert gas welding, J. Mater. Process. Technol. 222 (August) (2015) 381–390.

[52] K. Derekar, J. Lawrence, G. Melton, A. Addison, X. Zhang, L. Xu, Influence of Interpass Temperature on Wire Arc Additive Manufacturing (WAAM) of Aluminium Alloy Components, MATEC Web Conf. 269 (2019) 05001.

[53] C.R. Cunningham, J.M. Flynn, A. Shokrani, V. Dhokia, S.T. Newman, Invited review article: Strategies and processes for high quality wire arc additive manufacturing, Additive Manufacturing 22 (August) (2018) 672–686.

[54] J.P. Oliveira, T.G. Santos, R.M. Miranda, Revisiting fundamental welding concepts to improve additive manufacturing: From theory to practice, Prog. Mater. Sci. 107 (January) (2020) 100590.

[55] J.J. Lin, et al., Microstructural evolution and mechanical properties of Ti-6Al-4V wall deposited by pulsed plasma arc additive manufacturing, Mater. Des. 102 (July) (2016) 30–40.

[56] Z. Li, et al., Reducing arc heat input and obtaining equiaxed grains by hot-wire method during arc additive manufacturing titanium alloy, Mater. Sci. Eng. A 742 (January) (2019) 287–294.

[57] F. Montevecchi, G. Venturini, N. Grossi, A. Scippa, G. Campatelli, Heat accumulation prevention in Wire-Arc-Additive-Manufacturing using air jet impingement, Manuf. Lett. 17 (August) (2018) 14–18.

[58] E.M. Van Der Aa, Local cooling during welding: Prediction and control of residual stresses and buckling distortion, Delft University of Technology, 2007.

[59] X. Lu, Y.F. Zhou, X.L. Xing, L.Y. Shao, Q.X. Yang, S.Y. Gao, Open-source wire and arc additive manufacturing system: formability, microstructures, and mechanical properties, Int. J. Adv. Manuf. Technol. 93 (5–8) (2017) 2145–2154.

[60] Y. Chen, et al., Dendritic microstructure and hot cracking of laser additive manufactured Inconel 718 under improved base cooling, J. Alloys Compd. 670 (June) (2016) 312–321.

[61] B. Wu, Z. Pan, D. Ding, D. Cuiuri, H. Li, Z. Fei, The effects of forced interpass cooling on the material properties of wire arc additively manufactured Ti6Al4V alloy, J. Mater. Process. Technol. 258 (August) (2018) 97–105.

[62] B. Wu, et al., Mitigation of thermal distortion in wire arc additively manufactured Ti6Al4V part using active interpass cooling, Sci. Technol. Weld. Join. 24 (July 5) (2019) 484–494.

[63] R. Thavamani, V. Balusamy, J. Nampoothiri, R. Subramanian, K.R.R. Ravi, Mitigation of hot cracking in Inconel 718 superalloy by ultrasonic vibration during gas tungsten arc welding, J. Alloys Compd. 740 (April) (2018) 870–878.

[64] C. Hua, H. Lu, C. Yu, J.-M. Chen, X. Wei, J.-J. Xu, Reduction of ductility-dip cracking susceptibility by ultrasonic-assisted GTAW, J. Mater. Process. Technol. 239 (January) (2017) 240–250.

[65] N. Anbarasan, N. Narein, S. Jerome, Influence of Mechanical Arc Oscillation on the Microstructural and Mechanical Properties of Inconel 718 Welds, Trans. Indian Inst. Met. 72 (June 6) (2019) 1541–1544.

[66] X. Yu, et al., Reducing hot cracking tendency of dissimilar weld overlay by magnetic arc oscillation, Mater. Sci. Technol. (United Kingdom) 30 (July 8) (2014) 930–937.

[67] P.A. Colegrove, et al., Microstructure and residual stress improvement in wire and arc additively manufactured parts through high-pressure rolling, J. Mater. Process. Technol. 213 (October 10) (2013) 1782–1791.

[68] R. Sun, et al., Microstructure, residual stress and tensile properties control of wire-arc additive manufactured 2319 aluminum alloy with laser shock peening, J. Alloys Compd. 747 (May) (2018) 255–265.

[69] M.A. Somashekara, M. Naveenkumar, A. Kumar, C. Viswanath, S. Simhambhatla, Investigations into effect of weld-deposition pattern on residual stress evolution for metallic additive manufacturing, Int. J. Adv. Manuf. Technol. 90 (5–8) (2017) 2009–2025.

[70] G. Venturini, F. Montevecchi, A. Scippa, G. Campatelli, Optimization of WAAM Deposition Patterns for T-crossing Features, Procedia CIRP 55 (2016) 95–100.

[71] F. Michel, H. Lockett, J. Ding, F. Martina, G. Marinelli, S. Williams, A modular path planning solution for Wire + Arc Additive Manufacturing, Robot. Comput. Integr. Manuf. 60 (December) (2019) 1–11.

[72] H. Lockett, J. Ding, S. Williams, F. Martina, Design for wire + Arc additive manufacture: Design rules and build orientation selection, J. Eng. Des. 28 (September 7–9) (2017) 568–598.

[73] D. Yang, G. Wang, G. Zhang, Thermal analysis for single-pass multi-layer GMAW based additive manufacturing using infrared thermography, J. Mater. Process. Technol. 244 (June) (2017) 215–224.

2020-09-11

Effect of crack-like defects on the fracture behaviour of Wire + Arc additively manufactured nickel-base Alloy 718

Seow, Cui Er

Elsevier